Materials Science & Engineering A 861 (2022) 144317

Contents lists available at ScienceDirect

Materials Science & Engineering A

journal homepage: www.elsevier.com/locate/msea

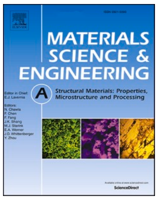

The conjoint influence of oxygen and hot extrusion on microstructure and mechanical properties of a powder metallurgy processed aluminum alloy

Weihao Han [a], Cunguang Chen [a,b,*], Pei Li [a], Yang Li [a], Guoping Su [a,c], Chunfang Sun [a],
Fang Yang [a,b,**], Alex A. Volinsky [d], Zhimeng Guo [a,b]

[a] Institute for Advanced Materials and Technology, University of Science and Technology Beijing, Beijing, 100083, China
[b] Shunde Innovation School, University of Science and Technology Beijing, Foshan, 528399, China
[c] AlTi Advanced Materials (Xianghe) Co. Ltd, Langfang, 065400, China
[d] Department of Mechanical Engineering, University of South Florida, 4202 E. Fowler Ave., ENG 030, Tampa, FL, 33620, USA

ARTICLE INFO

Keywords:
Oxygen content
Al–Zn–Mg–Cu alloy
Powder metallurgy
Hot extrusion
Mechanical properties

ABSTRACT

In this paper, Al-8.3Zn-2.3Mg-2.5Cu alloys with different oxygen contents were prepared through complex techniques including blending or ball milling, cold isostatic pressing, vacuum sintering, hot extrusion, and heat treatment, and their microstructure and mechanical properties were investigated. For the samples containing 0.15 wt% and 0.33 wt% oxygen, the sintered density values are 99.1% and 98.7% of the theoretical density, and the corresponding average grain sizes are 5.60 μm and 4.83 μm. After heat treatment, the average grain sizes of the samples with 0.15 wt% oxygen subjected to the extrusion ratios of 4:1, 9:1, and 17:1 are 5.17 μm, 4.28 μm and 3.83 μm, respectively, and the corresponding yield strengths are 607 MPa, 615 MPa, and 621 MPa. Moreover, the {111}<112> deformation texture changes to {001}<001> and {001}<111> recrystallization textures. In contrast, for the extruded sample (9:1 extrusion ratio) with 0.33 wt% oxygen, the grains are finer, and static recrystallization barely occurs with little variation in texture after heat treatment. This is due to the increase in content of thermostable γ-Al$_2$O$_3$ particles. Accordingly, the sample with high oxygen content exhibits excellent comprehensive mechanical properties with the ultimate tensile strength of 719 MPa, yield strength of 690 MPa, and elongation of 11.5%. Regarding the strengthening mechanism, apart from the common precipitation strengthening, the contributions of dislocation strengthening and grain boundary strengthening are greater in the 0.33 wt% oxygen alloy than in the 0.15 wt% oxygen alloy. This is due to the pinning effect of γ-Al$_2$O$_3$ particles on dislocations and grain boundaries.

1. Introduction

With the aggravation of the global energy crisis and the call for energy conservation and emission reduction [1], the demand for lightweight and high-strength structural materials, especially aluminum alloy-based structural materials, is becoming increasingly urgent in various energy-intensive fields such as aerospace and transportation [2]. Al–Zn–Mg–Cu alloy has the highest strength among aluminum alloys, and is mainly used in aircraft skins, beams, rivets and other applications. In recent years, further enhancing the strength of Al–Zn–Mg–Cu alloy to achieve weight reduction of aerospace components has become a research focus [3]. The main strengthening mechanisms of Al–Zn–Mg–Cu alloys are precipitation hardening and grain refinement [4–6]. To improve the mechanical properties of Al–Zn–Mg–Cu alloys, previous research has focused on increasing the content and types of alloying elements to obtain more precipitation phases and severe plastic deformation (SPD) to refine the grain structure [7–10].

Regarding the precipitation behavior of Al–Zn–Mg–Cu alloys, the common precipitation sequence during aging treatment is as follows: α-supersaturated solid solution → GP (I, II) zones→ η' phase → η ($MgZn_2$) phase [11]. Previous studies [12–15] have shown that uniform, fine and high-density intragranular precipitates are necessary for achieving high strength. Therefore, increasing the content of zinc, magnesium and copper can greatly improve the strength of alloys due to precipitation hardening. Li et al. [16] successfully prepared Al–11Zn-xMg-yCu alloy by a spray deposition method. During heat

---

* Corresponding author. Institute for Advanced Materials and Technology, University of Science and Technology Beijing, Beijing, 100083, China.
** Corresponding author. Institute for Advanced Materials and Technology, University of Science and Technology Beijing, Beijing, 100083, China.
E-mail addresses: cgchen@ustb.edu.cn (C. Chen), yangfang@ustb.edu.cn (F. Yang).

https://doi.org/10.1016/j.msea.2022.144317
Received 12 September 2022; Received in revised form 26 October 2022; Accepted 7 November 2022

treatment, abundant secondary phases were dissolved into the matrix and thereafter reprecipitated to form ultrafine strengthening particles after artificial aging, reaching the tensile strength of 800 MPa. Allah et al. [17] prepared Al-11.3Zn-2.65 Mg–1Cu alloy by spray deposition and obtained similar results. Due to the massive precipitation of the η' phase, the alloy achieved an ultra-high yield strength of 807 MPa. However, despite showing appealing strength, the elongation of the alloys sharply dropped to less than 8%. Furthermore, such high alloy content means high cost, while the microstructure and densification of the core and outer layers of the large ingot manufactured by spray deposition are inconsistent [18].

Numerous articles have verified the effective strength enhancement of Al–Zn–Mg–Cu alloys by grain refinement. After decades of development, various SPD technologies, such as equal channel angular pressing (ECAP) [19], high-pressure torsion (HPT) [20], multi-direction forging (MDF) [21], and accumulative roll bonding (ARB) [22,23], have been used for pure aluminum and its alloys to obtain ultra-fine grain structure. Wang et al. [24] designed a fine-grained structure of commercial 7055 aluminum alloy by the ECAP process, and found that its yield strength was increased by more than 41%, and the elongation dropped only slightly. Markushev et al. [25] reported that the Al-8.1Zn-2.2Mg-2.3Cu-0.1Zr-0.27Sc-0.1Mn alloy subjected to HPT showed the most developed nanostructure with a grain size of 80 ± 20 nm, and the ultimate tensile strength of over 1000 MPa. Unfortunately, the SPD technique can currently produce only small-sized pieces of products, such as wires, strips, and thin plates, instead of large billets.

Breaking the trade-off relation between microstructure uniformity, excellent performance and large size has always been the pursued goal for industrialization. In recent years, powder metallurgy has shown many advantages in solving these problems. Previous work reported the preparation of powder metallurgy Al–Zn–Mg–Cu alloys having 65 cm diameter, 1.7 m length, with ultra-fine grains and ultra-high strength [26]. Powder metallurgy aluminum alloys, also known as oxide dispersion strengthened (ODS) Al alloys, provide a new way for fine-grain strengthening [27–29]. Due to the dispersion enhancement effects of the Al_2O_3 nanoparticles, fine and even microstructure is obtained and the tensile strength is also improved by deformation and heat treatment. Similar to other ODS materials, such as ODS steel and Cu [30,31], the quantity and distribution of dispersoids largely dictate the mechanical properties of the aluminum alloys. According to the Orowan mechanism, low levels of oxygen cannot synthesize sufficient numbers of dispersion-strengthening Al_2O_3 particles to hinder dislocation movement and grain boundary migration. On the contrary, high oxygen content can result in the formation of large Al_2O_3 particles, drastically reducing the elongation of alloys [32,33]. Particularly for the powder metallurgy Al–Zn–Mg–Cu alloy, the contribution of multiple precipitated phases to the properties must be considered as well. So far, few studies have been reported on the effects of oxygen content on the microstructure and physical properties of powder metallurgy Al–Zn–Mg–Cu alloys.

In this work, Al–Zn–Mg–Cu powders with two oxygen levels (0.15 wt% and 0.33 wt%) were designed and prepared by V-type blending and rotary ball-milling, respectively. Cold isostatic pressing and vacuum sintering were carried out to obtain dense powder metallurgy Al–Zn–Mg–Cu alloys. Powder metallurgy Al–Zn–Mg–Cu alloy with 0.15 wt% oxygen was hot extruded with different extrusion ratios of 4:1, 9:1, and 17:1 to study the effects of deformation on the microstructure and mechanical properties, while that with 0.33 wt% oxygen was deformed with the extrusion ratio of 9:1. Heat treatment, including solid solution and artificial aging, was thereafter performed under the same conditions. The effects of extrusion ratio and oxygen content on microstructure evolution and mechanical properties of the alloys, and the related strengthening mechanisms were investigated. The results show that a large number of stable and fine alumina particles exist in the powder metallurgy Al–Zn–Mg–Cu alloy with high oxygen content. These alumina particles can prevent the migration of dislocations and grain boundaries. The processed structure, that is, the deformed texture, is thus retained to the greatest extent, and the grain size is maintained at 2–3 μm even after high temperature heat treatment. As a result, the powder metallurgy Al–Zn–Mg–Cu alloy with high oxygen content has the tensile strength of more than 700 MPa with only 9:1 extrusion ratio, and has the considerable elongation. Compared with other processes for improving the performance of Al–Zn–Mg–Cu alloy mentioned above, this process not only has low cost and short operation time, but can also be used to prepare large-sized aluminum alloy billets. Due to these characteristics of easy industrialization, powder metallurgy high-strength Al–Zn–Mg–Cu alloys have excellent application potential.

2. Experimental procedure

Commercial aluminum ($D_{50} = 20$ μm), Al–50Zn alloy ($D_{50} = 18$ μm), magnesium ($D_{50} = 80$ μm) and copper ($D_{50} = 7$ μm) powders were used as raw materials. The morphology of all powders has been reported in previous research [26]. To obtain different oxygen contents, the nominal composition Al-8.3Zn-2.3Mg-2.5Cu (mass fraction) powders were prepared by V-type blending and rotary ball-milling, respectively. The processes of blending and ball milling were carried out in a V-type mixer and drum ball mill, respectively, with a rotation speed of 240 rpm for 5 h. Different from the blending process, steel balls with a ball-to-material ratio of 9:1 were added in the drum ball mill to increase the oxygen content of powders. All powders were then compacted at 180 MPa pressure for 2 min in a rubber mold by a cold isostatic press. The green compact was sintered under vacuum at 580 °C for 2 h to obtain Al alloy ingots with 210 mm diameter and 1.2 m length. The alloys prepared by blending and ball milling were named blended and ball-milled, respectively. The detailed contents of zinc, magnesium, copper, and oxygen of the two sintered alloys are listed in Table 1. Hot extrusion was subsequently conducted at 420 °C with a speed of 0.3 mm/s. The blended plates were squeezed out with the extrusion ratio of 4:1 (blended-4), 9:1 (blended-9), and 17:1 (blended-17), while the ball-milled plates with the extrusion ratio of 9:1 (ball-milled-9) were obtained at the same conditions. The thicknesses of blended-4, blended-9 (ball-milled-9), and blended-17 plates were 13.7 mm, 24 mm, and 50.5 mm, respectively, and the width of all extruded plates was 135 mm. Afterward, T6 heat treatment was carried out, including solution treatment at 470 °C for 120 min and immediate quenching into water at room temperature, and finally artificial aging at 120 °C for 24 h. The schematic diagram of the preparation process is shown in Fig. 1.

Microstructure examinations of the sintered and extruded samples were performed by field-emission scanning electron microscope (FESEM, SUPRA 55, Carl-Zeiss, Germany) operated at 15 kV, electron backscatter diffraction (EBSD) operated at 20 kV and transmission electron microscope (TEM, Tecnai G2 F30, FEI, USA) operated at 200 kV. The composition of the alloy precipitates was analyzed by energy dispersive spectrometry (EDS). To analyze the phases of the sintered, extruded, and heat-treated samples, X-ray diffraction (XRD, Rigaku TTR III, Japan) was performed using monochromatic Cu-Kα radiation with the X-ray wavelength of 0.154 nm at 40 kV and 150 mA. The Archimedes method was used to measure the density of each sample (ASTM B962-13). Samples for tensile tests were machined into a dog-bone shape with 5 mm diameter, 80 mm total length, and 25 mm gauge length. At least six tensile samples from blended and ball-milled plates were prepared for tensile tests performed at room temperature and 0.5

Table 1
Composition of the blended and ball-milled alloys.

Specimen	Composition in wt.%				
	O	Zn	Mg	Cu	Al
Blended alloy	0.15	8.16	2.28	2.48	Bal.
Ball-milled alloy	0.33	8.12	2.27	2.49	Bal.

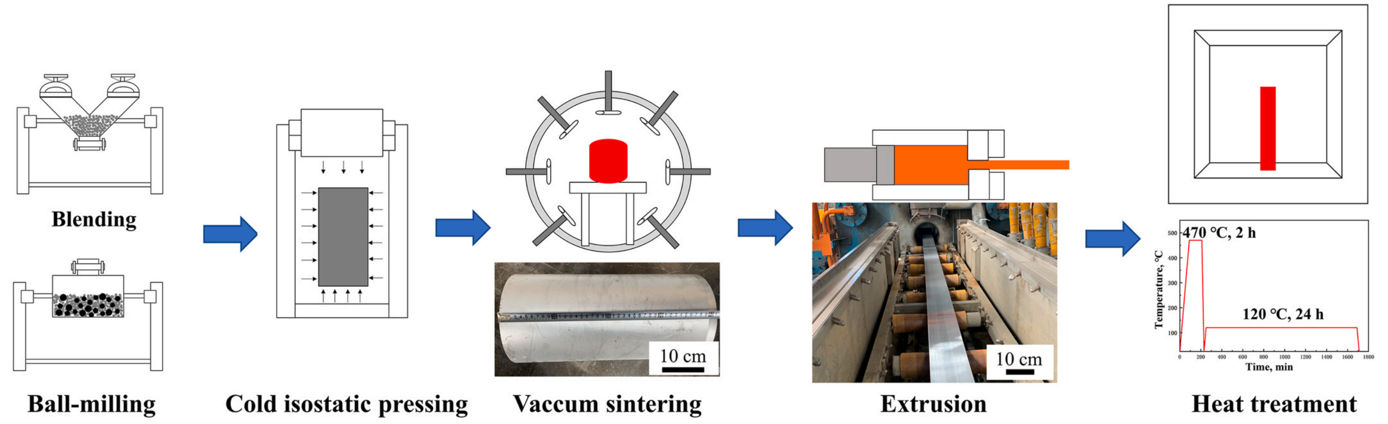

Fig. 1. Schematic diagram of the preparation process of investigated samples.

mm/min speed.

3. Results

3.1. Microstructure of sintered alloys

The powder particles remain nearly spherical after V-type blending, as shown in Fig. 2, while the morphology of powder particles presents an irregular shape after ball milling. Due to the collision and friction between the steel balls and the aluminum powder particles during the ball milling process, the powder undergoes plastic deformation. The impact of the steel balls on the powder is relatively weak with the ball-to-material ratio of 9:1. This causes a few powder particles to appear flaky or refined, only changing their surface morphology. The oxygen content is determined to be 0.15 wt% for the blended sintered alloy and 0.33 wt% for the ball-milled sintered alloy, as presented in Table 1. The increase in oxygen content can be attributed to the immediate oxidation of powder particles subjected to ball milling.

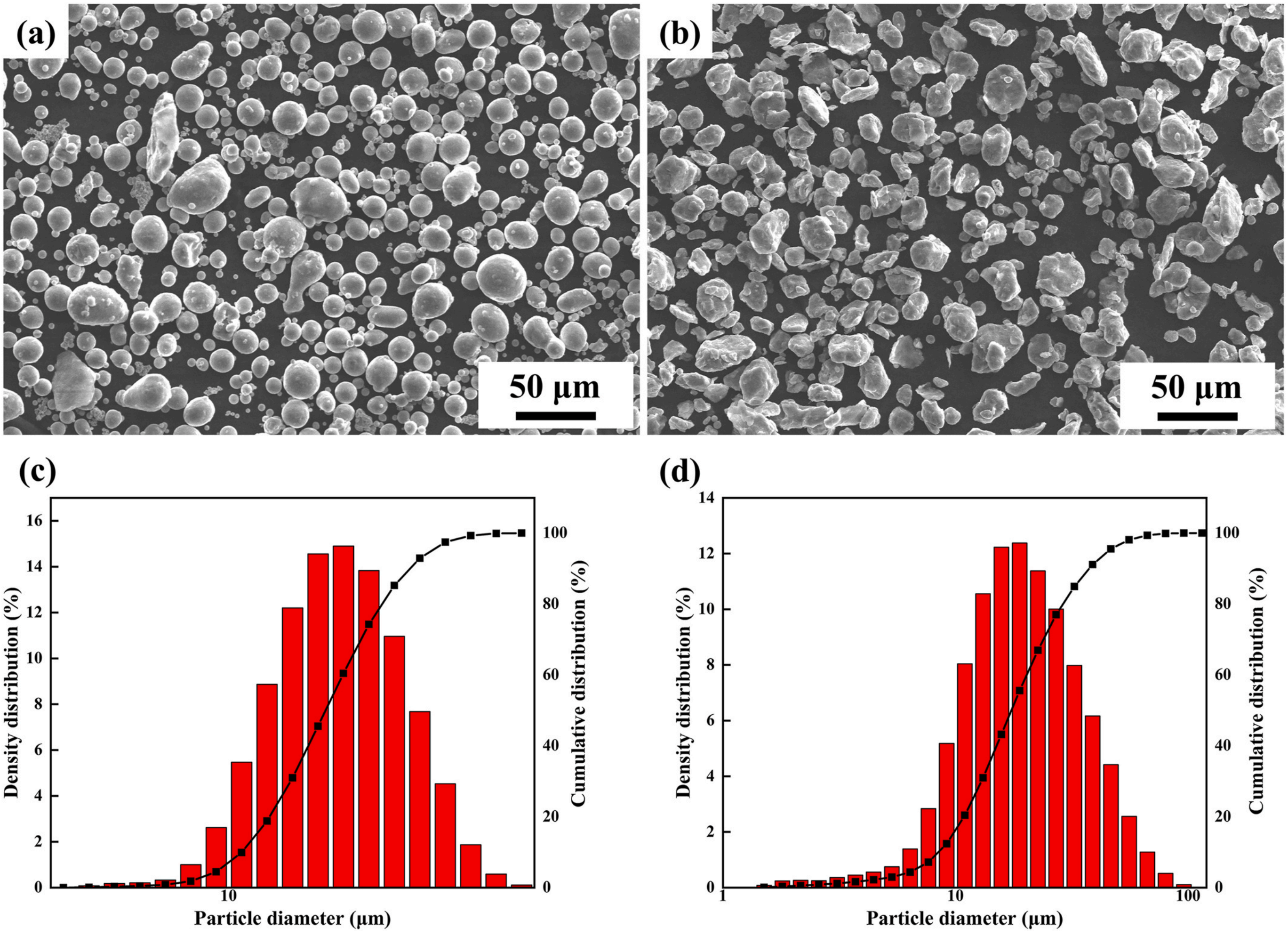

Fig. 2. SEM image and particle size distribution of Al-8.3Zn-2.3Mg-2.5Cu powder processed by (a) and (c) blending, (b) and (d) ball milling.

The microstructures of blended and ball-milled alloys sintered under vacuum are shown in Fig. 3. The relative density values of blended and ball-milled sintered alloys calculated by Archimedes' method are 99.1% and 98.7% of the theoretical density, respectively. The pores of the ball-milled alloy in Fig. 3(b) are larger than those of the blended alloy in Fig. 3(a). The reason is that the oxidation of the powder particles during ball milling causes a decrease in activity and hinders the sintering process. Nevertheless, the pore size of both sintered alloys is relatively small. It should be noted that such a high sintered density for powder metallurgy Al–Zn–Mg–Cu alloy has been rarely reported. This result may be due to the addition of zinc element. It is generally considered that zinc is a poor sintering aid, and its high vapor pressure also gives rise to additional porosity in these alloys, particularly when elemental powders are used [34]. Therefore, it is suggested to use master alloy powders [35], such as Al–50Zn alloy powder used in this work.

After sintering, there are a large number of secondary phases distributed at the grain boundaries inside the blended and ball-milled alloy samples. This is due to spontaneous formation of grain boundary segregation. The boundary structure defects are more than those in the crystal, the energy of solute atoms in the crystal is higher than that in the grain boundary, and the system energy is reduced through segregation. On the other hand, comparing Fig. 3 with Fig. 2, it can be found that the shape and size of the crystal grains in the precipitation phase are consistent with those of the original powder particles. This phenomenon indicates that it is difficult for the grains to grow beyond the boundaries of the original powder particles even at the high sintering temperature of 580 °C. The fundamental reason for this phenomenon is that the alumina film existing at the boundary of the original powder particles is stable. Although it is broken during the pressing process, it still exists after sintering. This broken oxide film hinders the migration of grain boundaries.

The SEM images at higher magnification and the corresponding EDS mapping results of the two sintered alloys are shown in Fig. 4. Although the raw materials are aluminum powder, magnesium powder, copper powder and Al–Zn50 powder, the diffusion of each element is very uniform after sintering. Moreover, the distribution of each alloy element is macroscopic. A large number of secondary phases dominated by $MgZn_2$ are enriched at the grain boundaries. However, these secondary phases belong to the micro-scale precipitation, which can be completely dissolved into the matrix after solution treatment [16]. The elemental analysis shows that magnesium, zinc, copper, and O are enriched at the boundaries of the powder particles. By comparison, the oxygen content at the boundaries of the powder particles after ball milling is significantly higher than that after blending, which is consistent with the relative density results. The XRD results of the two sintered powders are shown in Fig. 4(c). The $MgZn_2$ reflection is apparent for the two sintered alloys, confirming the formation of the $MgZn_2$ precipitated phase.

EBSD analysis was performed to characterize the microstructure in terms of the grain size, texture, and stress distribution of sintered aluminum alloys after cold isostatic pressing (CIP), as shown in Fig. 5. It can be seen from the grain orientation images (OIMs) in Fig. 5(a) and (e) that the microstructures of both alloys present no preferred grain orientation. In the CIP process, aluminum powder first undergoes particle rearrangement and then plastic deformation under 180 MPa isostatic pressure, because aluminum with a face-centered cubic (FCC) crystal structure is prone to plastic deformation. After sintering at 580 °C, recrystallization occurs and a large number of recrystallized grains are formed. However, due to the binding of the original grain boundaries, the recrystallized grains grow into grains corresponding to the prior particle boundaries, which are bound by high-angle grain boundaries (HAGBs, >15°), marked in green. This result is consistent with Fig. 2. Moreover, a large number of low-angle grain boundaries (LAGBs, 2–15°) exist inside the original powder particles, marked with red color in Fig. 5(b) and (f). Since the original adjacent particles are randomly arranged, they are more inclined to form an equiaxed grain structure from a macroscopic point of view, that is, adjacent particles tend to form HAGBs. In addition, the broken oxide film at the original grain boundary during the sintering process hinders the migration of the grain boundary, so the HAGB is distributed at the original grain boundary after sintering. Comparing Fig. 5(b) and (f), it is found that the ball-milled alloy has fewer LAGBs, which is due to the fact that some alumina particles are kneaded into the powder during the ball milling process. These alumina particles hinder the migration of dislocations during the subsequent sintering process to form a polymorphic structure. Hence, the alumina particles prevent the eventual formation of subcrystals. However, there are very few alumina particles in the blended alloy powders, and the internal dislocations can develop into subgrains.

As seen from the kernel average misorientation (KAM) maps in Fig. 5 (c) and (g), the locations of HAGBs exhibit high density of geometrically necessary dislocations (GNDs), with the red color representing the intense deformation region. The stress levels at the prior particle boundaries are higher than those inside the particles. This phenomenon can be attributed to the oxide film and secondary phases around the prior particle boundaries that disturb the dislocation movements and grain boundary migration. The grain size distribution and average grain size are shown in Fig. 5(d) and (h). A large number of crystalline grains of blended and ball-milled sintered alloys are below 5 μm. The average grain size of the blended sintered alloy (5.60 μm) is slightly larger than that of the ball-milled alloy (4.83 μm). Other literature results [36] also pointed out that after CIP, a large amount of the oxide film was broken, which promoted the sintering behavior. The dispersed alumina film hinders the growth of grains. In this paper, only the surface morphology of the ball-milled powder is changed, but no obvious particle refinement occurs. Therefore, there is more alumina after ball milling, but the particle size is similar to that before ball milling. This is the reason why

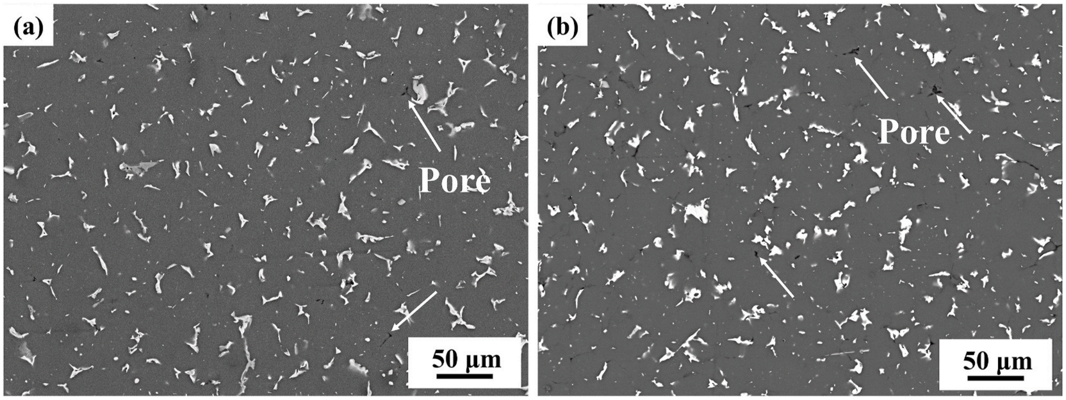

Fig. 3. SEM images of the sintered Al-8.3Zn-2.3Mg-2.5Cu alloy obtained by (a) blending, and (b) ball milling.

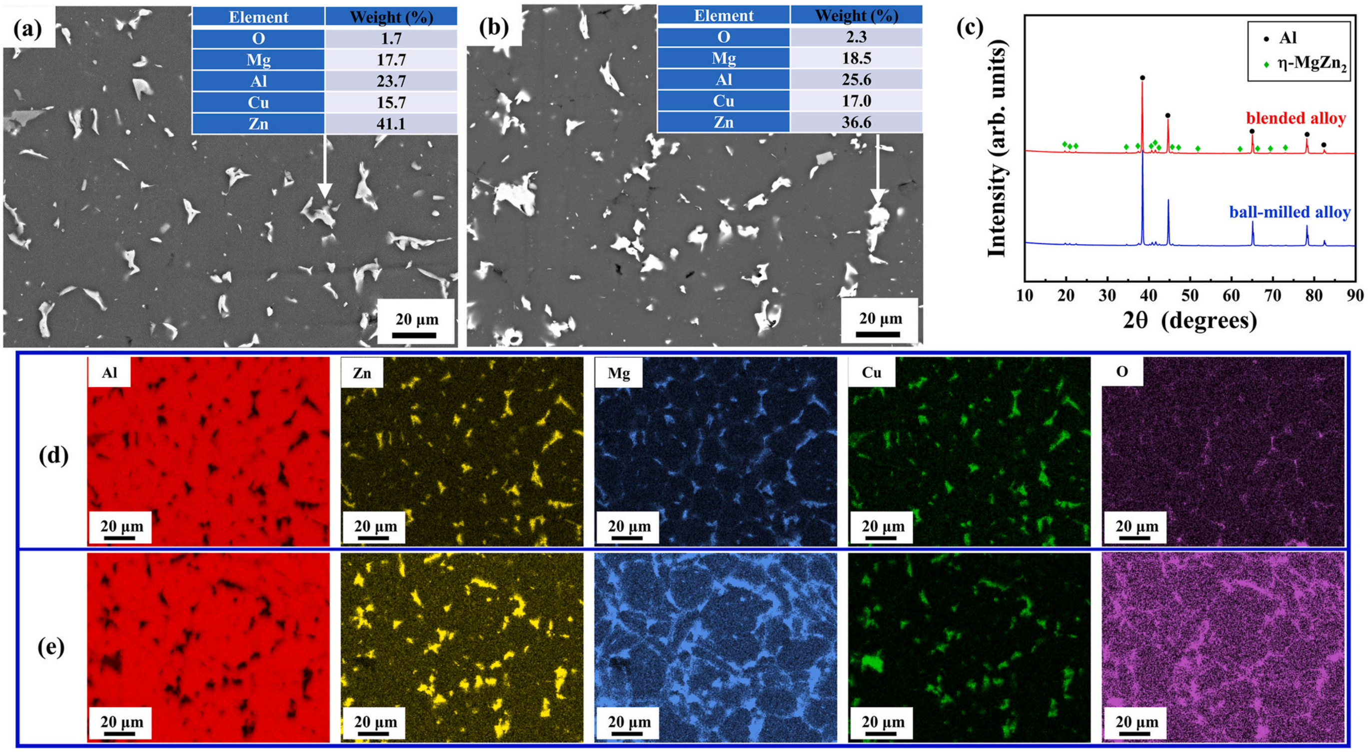

(a)

Element	Weight (%)
O	1.7
Mg	17.7
Al	23.7
Cu	15.7
Zn	41.1

(b)

Element	Weight (%)
O	2.3
Mg	18.5
Al	25.6
Cu	17.0
Zn	36.6

Fig. 4. SEM images and EDS results of the secondary phase of sintered (a) blended and (b) ball-milled alloys, (c) XRD patterns of sintered blended and ball-milled alloys, and EDS elemental maps of sintered (d) blended and (e) ball-milled alloys.

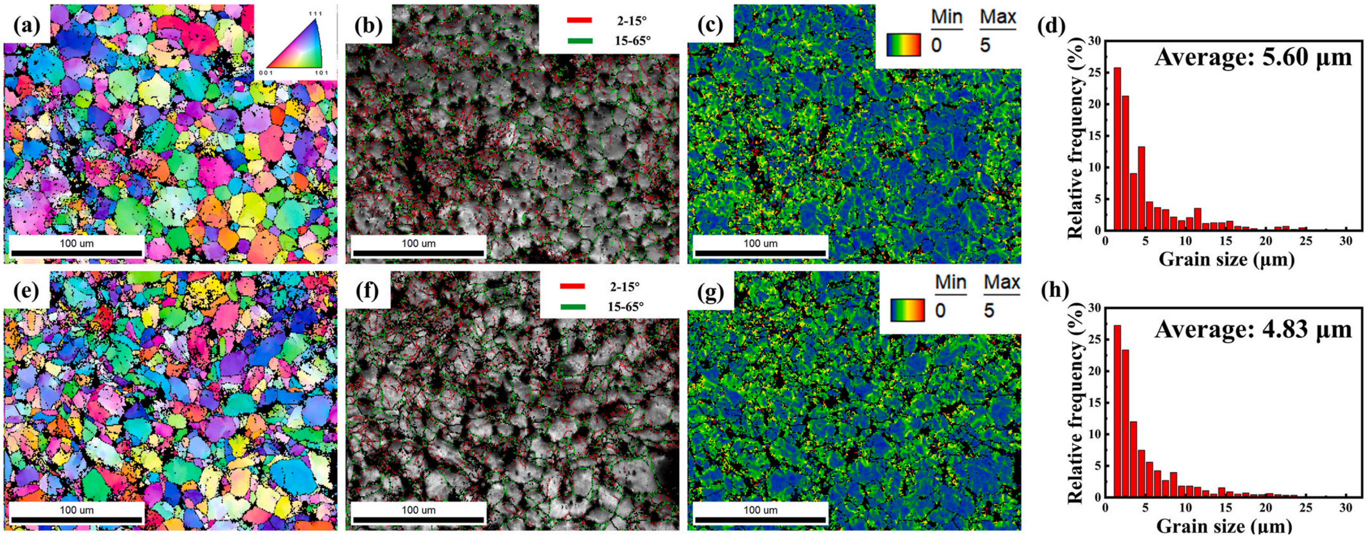

Fig. 5. EBSD images of vacuum sintered alloys and the orientation image maps of the (a) blended and (e) ball-milled alloys; grain boundary maps of the (b) blended and (f) ball-milled alloys; the kernel average misorientation maps of (c) blended and (g) ball-milled alloys; the grain size distribution of (d) blended and (h) ball-milled alloys.

the grain size of the ball-milled alloy is slightly smaller than that of the blended alloy.

3.2. Microstructure of extruded and heat-treated alloys

SEM images of the microstructures of extruded and corresponding heat-treated alloys are shown in Fig. 6. The microstructures of the secondary phase distribution (white spots) for the alloys with different extrusion ratios are displayed in Fig. 6(a–c). The secondary phases at the grain boundaries and inside the grains are fractured into fine particles by shear stress during the extrusion. For the extrusion ratio of 4:1, a large number of rough particles are distributed along the grain boundaries, as seen in Fig. 6(a). The coarse particles become smaller and more uniformly distributed in the matrix at a higher extrusion ratio, as seen in Fig. 6(b) and (c). After the T6 heat treatment, almost all visible large secondary phases in the extruded state disappear. Due to the solid solution treatment, the $MgZn_2$ phase is dissolved into the matrix. The reprecipitated phases during the subsequent aging at 120 °C for 24 h are not easily observed by SEM, as shown in Fig. 6(d–f). The detailed TEM analysis of the aged precipitates is presented next.

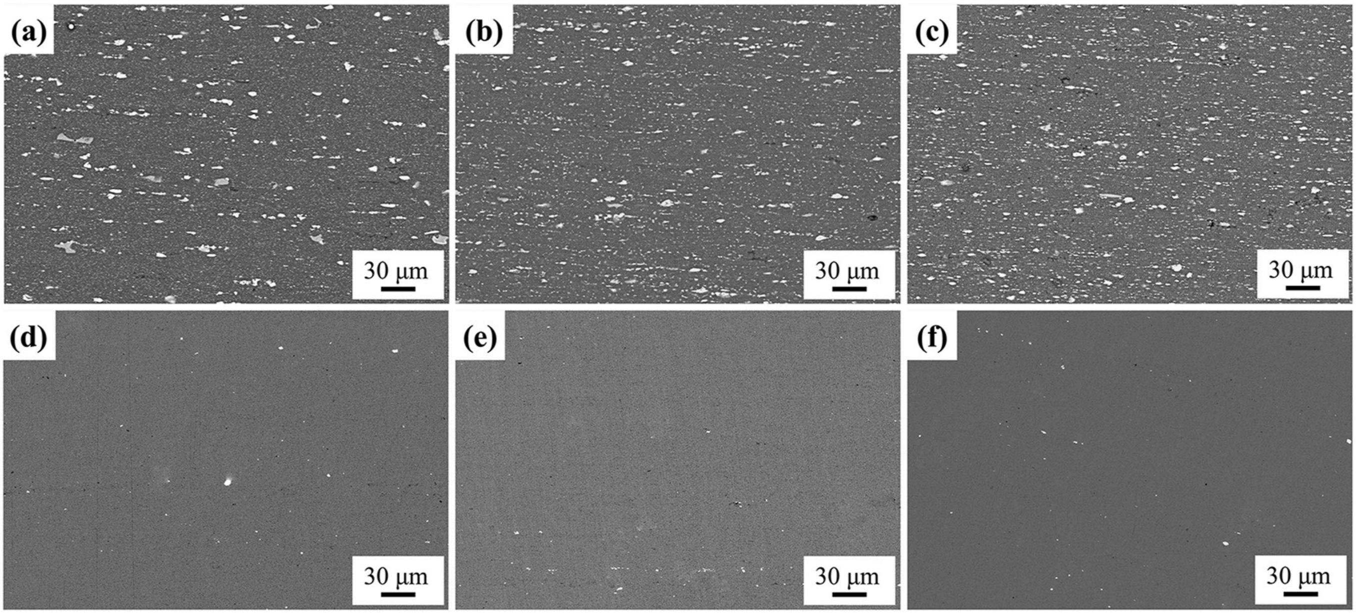

Fig. 6. SEM images of extruded alloys: (a) blended-4, (b) blended-9, (c) blended-17, and heat-treated alloys: (d) blended-4, (e) blended-9, (f) blended-17.

After the extrusion and heat treatment at 420 °C, the grains undergo dynamic and static recrystallization. The OIMs and embedded statistics of the grain size distribution for different deformation conditions are shown in Fig. 7(a–c). The grains are elongated along the extrusion direction after deformation. The average grain sizes after hot extrusion with extrusion ratios of 4:1, 9:1, and 17:1 are 2.78 μm, 2.56 μm, and 2.54 μm, respectively. The extrusion ratios of 4:1, 9:1, and 17:1 correspond to the deformation amounts of 75%, 89%, and 94%, respectively. The microstructure evolves from irregularly arranged dislocations into cellular and subcrystalline structures with strain. Then, subcrystalline growth occurs, and finally, dynamic recrystallization may occur. When the degree of deformation is low, a large number of dislocation lines are generated inside the grain, and the dislocations are entangled with each other, resulting in numerous cellular structures. The dislocation entanglement in the cell wall forms a network of lower energy dislocations that eventually becomes the subgrain boundary. When the degree of deformation reaches a certain value, the subgrains migrate through torsion or due to the energy gradient on both sides of the grain boundary. Eventually, the subgrains merge and grow, and then some subgrains become HAGBs, and dynamic recrystallization occurs. A large number of original grain boundaries protrude, which is conducive to the occurrence of grain boundary migration and induced dynamic recrystallization. The number fraction vs. misorientation angle charts of extruded and heat-treated blended alloys are shown in Fig. 8. It can be seen from Fig. 8(a–c) that there are numerous LAGBs in the three alloys, and the sub-crystals formed by dislocation merging are dominant in the whole

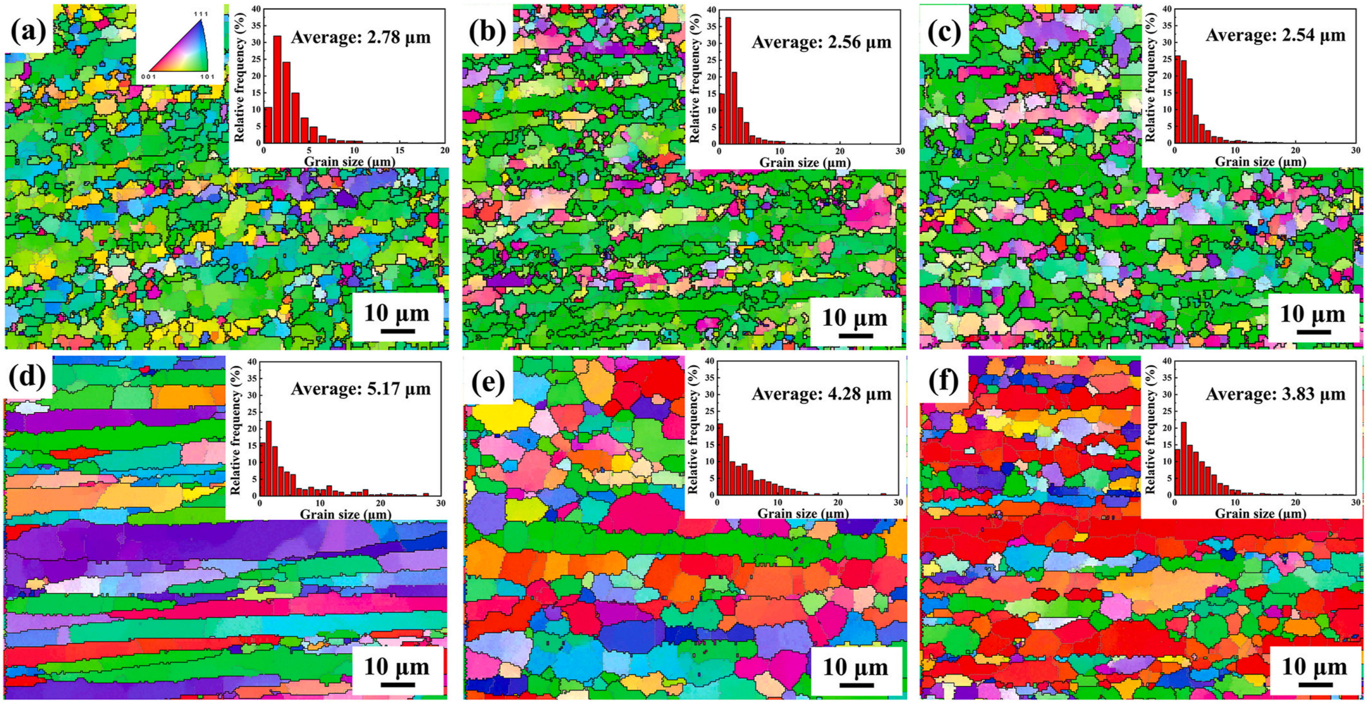

Fig. 7. OIMs of extruded alloys: (a) blended-4, (b) blended-9, (c) blended-17, and heat-treated alloys: (d) blended-4, (e) blended-9, (f) blended-17.

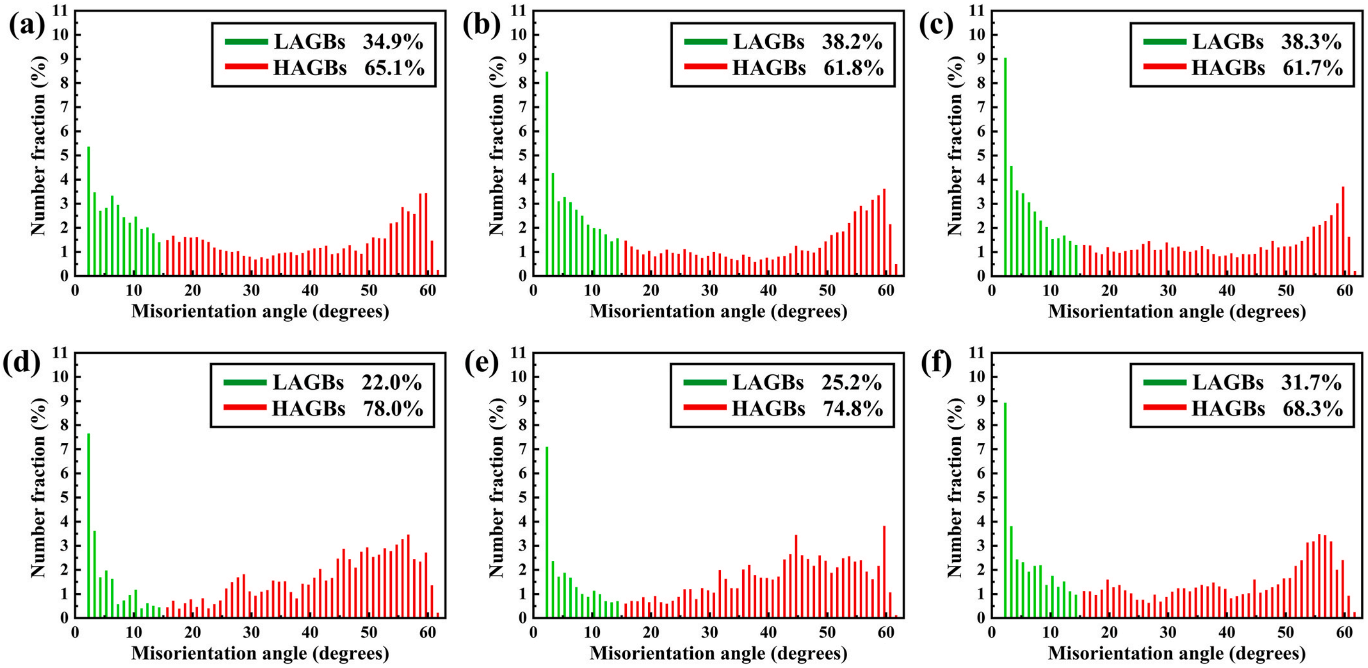

Fig. 8. The number fraction vs. misorientation angle of extruded alloys: (a) blended-4, (b) blended-9, (c) blended-17, and heat-treated alloys: (d) blended-4, (e) blended-9, (f) blended-17.

deformation process. Specifically, dynamic recovery mainly occurs and the degree of dynamic recrystallization is low. The deformation amount of blended-4 alloy is 75%, and there are fewer sub-crystals formed by dislocation merging. This is because a few subgrains are formed from dislocation cells at small deformation. The deformation amount of blended-9 sample is 89%. Compared with blended-4 sample, the number of LAGBs is increased, leading to more dislocations with deformation. Hence, more subgrains are formed by dynamic recovery. The LAGBs of blended-17 and blended-9 alloys are similar, while the blended-17 alloy has a larger amount of deformation, indicating that a small amount of dynamic recrystallization occurs in the blended-17 alloy. Regardless of the different extrusion ratios, the grain size at the three states is at the same level, because the grain size of the sintered alloys is refined to 5.60 μm. Meanwhile, the oxide film on the original grain boundary is broken after extrusion and the grain growth is thereby impeded. The OIMs and embedded statistics of grain size distribution after the T6 heat treatment (470 °C for 2 h + 120 °C for 24 h) are shown in Fig. 7(d–f), and the grain boundary statistics of the heat-treated samples are shown in Fig. 8(a–c).

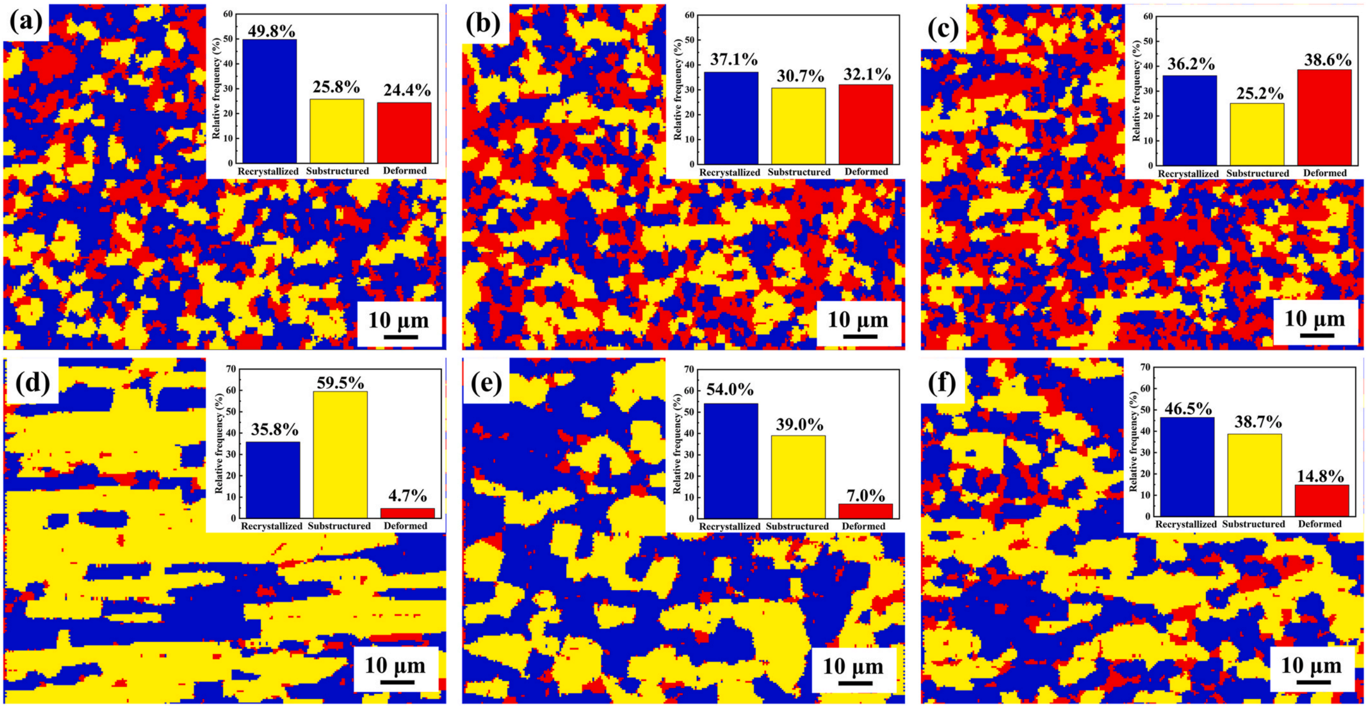

Fig. 9. The recrystallization maps of extruded alloys: (a) blended-4, (b) blended-9, (c) blended-17, and heat-treated alloys: (d) blended-4, (e) blended-9, (f) blended-17.

It can be seen from Fig. 8(d–f) that, after solution treatment, the number of LAGBs in all three alloys is less, while the number of HAGBs is increased. The deformation texture changes to recrystallized texture, indicating that the material experiences static recrystallization. It can be perceived that the number of recrystallized grains decreases with the extrusion ratio. After heat treatment, the average grain sizes of blended-4, blended-9, and blended-17 samples are 5.17 μm, 4.28 μm and 3.83 μm, increasing by 86%, 72%, and 51% compared with the extruded state, respectively. According to literature, the grains of the Al–Zn–Mg–Cu alloy prepared by the traditional casting process grow to more than 30 μm (also calculated by EBSD) after the extrusion and heat treatment [37].

The hot deformation is a combined process of work hardening, dynamic recovery, and recrystallization softening. The microstructure evolution results of blended-4, blended-9, and blended-17 samples before and after heat treatment obtained by the EBSD technique are depicted in Fig. 9. In the EBSD maps, the blue, yellow, and red regions represent the recrystallized, substructured, and deformed microstructures, respectively. The statistical results related to the volume fraction of the three kinds of microstructure are embedded in the corresponding map. As the extrusion ratio increases, the proportion of dynamic recrystallization decreases from 49.8% to 26.2%, while the proportion of the deformed microstructure rises from 24.4% to 38.6%, as shown in Fig. 9(a–c). The latter indicates that as the amount of deformation increases, the effect of work hardening is gradually greater than that of dynamic recovery and recrystallization, that is, the greater the deformation, the greater the deformation energy storage. During the solution treatment at 470 °C for 2 h, static recovery and recrystallization occur, and the proportion of all alloy deformed structures is reduced, mainly in the recovery and recrystallized structures. With the increase in deformation amount, the recrystallized structure of the alloy is continuously refined after heat treatment, and the grain refinement strengthening effect is continuously increased. This is consistent with the results in Figs. 7 and 8.

The following conclusions can be drawn by comparing the recovery and recrystallization of the three heat-treated alloys. The blended-4 alloy is dominated by statically recovered grains after heat treatment, and the dislocations merge with each other to form many subgrains. The reason for this phenomenon is that the deformation of the blended-4 alloy is small, and the distribution of oxide film after extrusion and crushing is not as uniform as that of blended-9 and blended-17. Although the oxide film can hinder the merging of subgrain boundaries, the subgrain formed by dynamic recovery has a recrystallized texture. This is the reason why the yellow regions are connected into sheets. The grains of blended-9 alloy are mainly recrystallized grains. Although the fracture of the oxide film is more uniform than that of blended-4 alloy, the deformation energy storage is more than that of blended-4 alloy, which reduces the recrystallization temperature. Therefore, after solid solution treatment at high temperature, the recrystallized grains of blended-9 alloy nucleate and grow in high-energy regions such as high-density dislocations, subgrain boundaries, and grain boundaries. The static recovery and recrystallized grain proportions of the blended-17 alloy are similar to those of the blended-9 alloy, which is determined by the distribution of the oxide film and the deformation energy storage. On the one hand, a larger extrusion ratio results in a more uniform distribution of the oxide film and a more pronounced pinning effect. On the other hand, the larger extrusion ratio leads to higher deformation energy storage, which increases the driving force for recrystallization.

The (111) pole figures (PFs) of extruded and heat-treated blended-4, blended-9, and blended-17 samples are shown in Fig. 10. The texture of the extruded sample is {111}<112>, and the texture intensity tends to increase. The texture can be regarded as a typical F texture [38]. After the T6 heat treatment, the texture orientation of blended-4 and blended-9 samples becomes strong {001}<001> and {001}<111>, while the texture of blended-17 sample becomes strong {001}<001> orientation and weak {001}<111> orientation. This is because the stored deformation energy is still relatively high after the hot deformation. Thus, the alloy undergoes static recrystallization after solid solution strengthening, resulting in the material texture change from deformation to recrystallization texture.

SEM images, EBSD results, and XRD patterns of the microstructure evolution of the ball-milled-9 alloy before and after heat treatment are shown in Fig. 11. The secondary phase distributions of the ball-milled-9 alloy in the extruded and heat-treated states are exhibited in Fig. 11(a) and (b). Compared with the blended-9 alloy, the secondary phase in the extruded state is smaller, and the texture after heat treatment is similar. The OIMs and grain statistics of the extruded and heat-treated ball-milled-9 alloy are presented in Fig. 11(c) and (d). It can be seen that the average grain size of the extruded ball-milled-9 alloy (2.17 μm) is

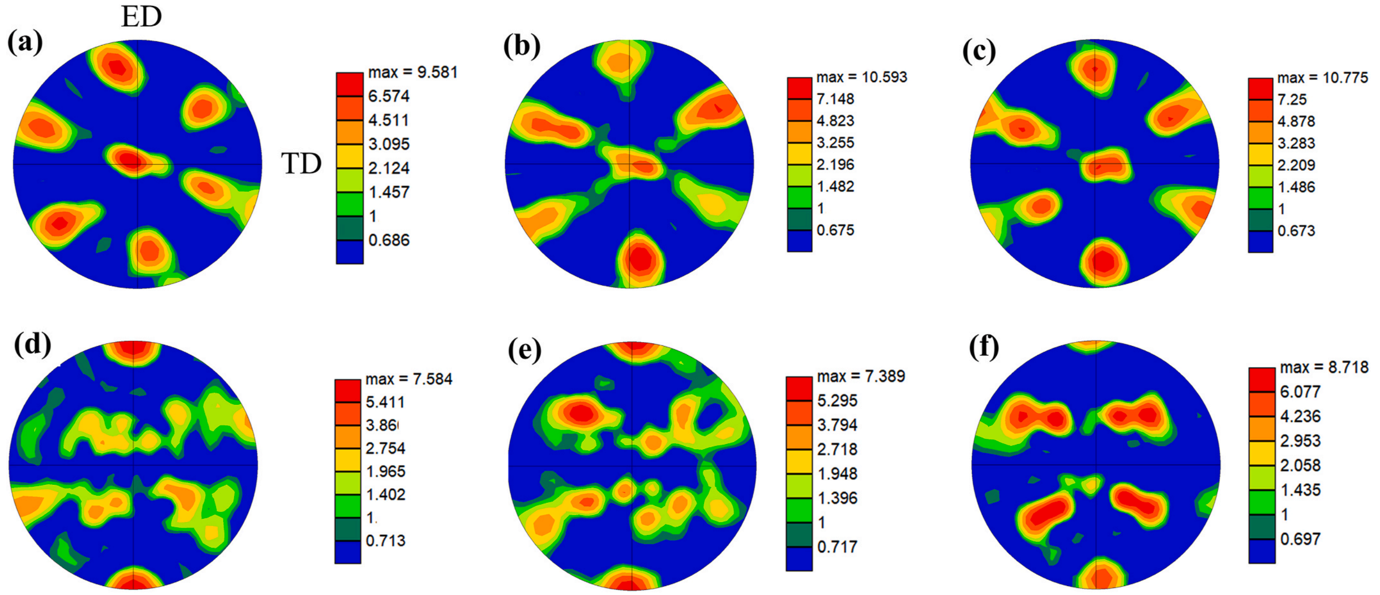

Fig. 10. The (111) PFs of as-extruded alloys: (a) blended-4, (b) blended-9, (c) blended-17, and as-heat treated alloys: (d) blended-4, (e) blended-9, (f) blended-17. (Extrusion direction named ED, thickness and width direction of the sheet named ND and TD, respectively).

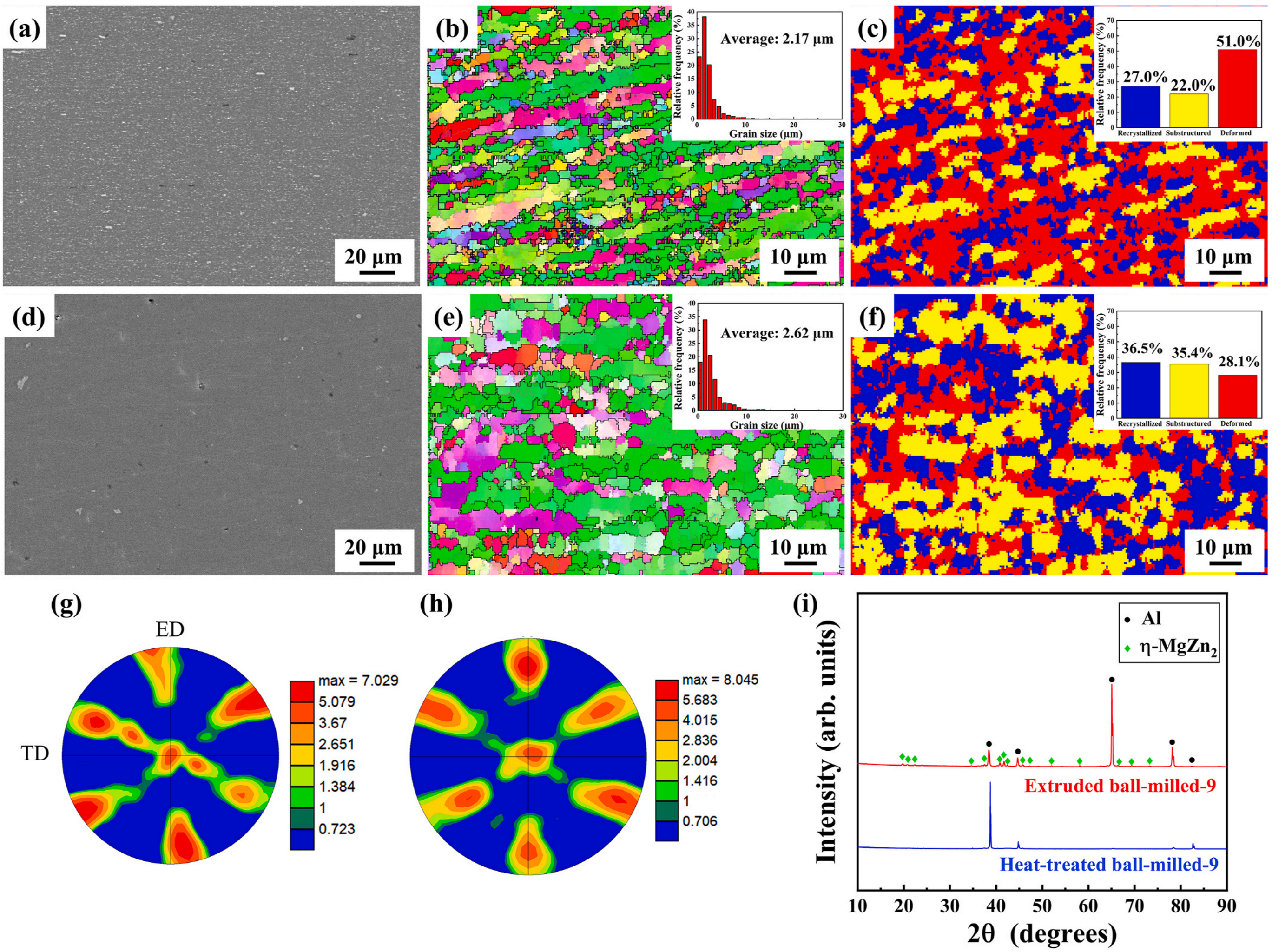

Fig. 11. (a) and (d) SEM images, (b) and (e) OIMs, (c) and (f) recrystallization maps, and PFs of (g) extruded ball-milled-9 alloy and (h) heat-treated ball-milled-9 alloy; (i) XRD patterns of extruded and heat-treated ball-milled-9 alloy.

slightly reduced compared to that of the blended-9 alloy (2.56 μm). After heat treatment, the average grain size of the ball-milled-9 alloy (2.62 μm) is not only significantly reduced compared to that of the blended-9 alloy (4.28 μm) but is even lower than that of the blended-17 alloy (3.83 μm). Partial maps of the recrystallized microstructure of the ball-milled-9 alloy in the extruded and heat-treated states are shown in Fig. 11(e) and (f). The extruded ball-milled-9 alloy has a large amount of distorted microstructure, and the proportion of deformed microstructure reaches 51%, indicating that the effect of dynamic recovery and recrystallization in this process is less than the effect of work hardening. Although the deformed texture after heat treatment tends to transform to the recovered and recrystallized structure, the deformed structure of ball-milled-9 alloy still accounts for 28.1% of the deformed microstructure of the blended-9 alloy (7%).

After ball milling, the number of oxide particles increases. This inhibits dynamic recovery and recrystallization of the alloy during deformation, and suppresses static recovery and recrystallization during heat treatment, thereby obtaining a finer texture. The texture of the extruded ball-milled-9 sample is the same as that of the blended-9 sample, i.e., the {111}<112> texture. The recrystallization behavior is restricted, corresponding to the same texture orientation and a minor increment of texture intensity. After heat treatment, the orientation of the ball-milled-9 sample remains unchanged, and the texture of the sheet remains the same. This is different from the texture change of the blended-9 sample, which also shows that the oxygen content inhibits the static recrystallization behavior. The XRD patterns of extruded and heat-treated ball-milled-9 alloy are shown in Fig. 11(i), demonstrating that the massive $MgZn_2$ particles in the matrix disappear after the T6 heat treatment.

TEM images of the oxide particles of the ball-milled-9 sample after heat treatment are displayed in Fig. 12. A large number of particles are uniformly distributed in the matrix with an irregular shape, as shown in Fig. 12(a), and the corresponding magnified microstructure of the red area is shown in Fig. 12(b). The size of the black particles ranges from 10 nm to 100 nm. Diffraction patterns containing several polycrystalline rings are also observed in Fig. 12(b), which are determined as γ-Al_2O_3 by comparison with the PDF#75–0921 standard card. The average particle size and volume fraction of γ-Al_2O_3 particles are listed in Table 2.

TEM images of intragranular and intergranular ball-milled-9 particles and the corresponding selected area electron diffraction (SAED) patterns after heat treatment are shown in Fig. 13. It can be seen from Fig. 13(a) that high-density ultra-fine precipitates are evenly distributed in the matrix. The precipitates remain continuous at the grain boundaries, and the width of precipitation free zones (PFZs) is about 20.5 nm. The micrograph of intragranular precipitates of heat-treated ball-milled-9 along the <011> Al direction is shown in Fig. 13(b). High-density flakes and/or elliptical-shaped finely dispersed phases are observed. Ultra-fine deposits with an average diameter of 5 nm are evenly distributed in the matrix. The average particle size and volume fraction of precipitated phases are listed in Table 2. The SAED patterns in

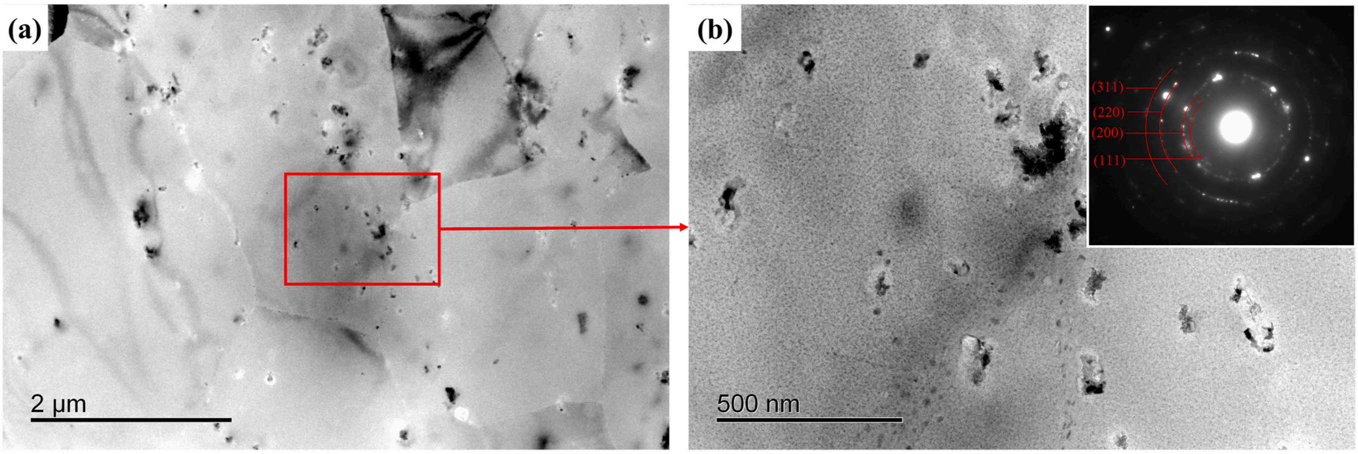

Fig. 12. TEM images of the oxide particles in the ball-milled-9 sample after heat treatment.

Table 2
Summary of the microstructural features of the ball-milled-9 alloy and quantitative analysis of the strengthening mechanisms.

		Parameter statistics	Mechanism	Value
Average grain size		2.62 μm	Grain boundary strengthening	74 MPa
Precipitates	Precipitate type	GP + η'		
	Average radius, *r*	2.23 nm	Precipitation strengthening	485 MPa
	Volume fraction, f_v	2.06%		
Dislocation density		4.6×10^{14} m^{-2}	Dislocation strengthening	101 MPa
γ-Al_2O_3	Average radius, *r*	36 nm		
	Volume fraction, f_v	0.52%		

different states are recorded to determine the nature of the deposits within the particles, as exhibited in Fig. 13(c). The main diffraction spots of the aluminum matrix are indexed as follows. The discrete diffraction points {1, (2n+1)/4, 0} in the <001> Al direction correspond to the Guinier-Preston zone I [39]. In addition, metastable η' phase appears at 1/3{220} and 2/3{220} positions of aluminum in <001> [40]. The high-resolution transmission electron microscope (HRTEM) image of the alloy is shown in Fig. 13(d), where the η'-phase is marked with white dotted rectangles.

3.3. *Mechanical properties*

The ultimate tensile strength, yield strength, and elongation of heat-treated blended-4, blended-9, blended-17, and ball-milled-9 alloys are shown in Fig. 14. As the extrusion ratio increases, the ultimate tensile strength and yield strength of blended-4, blended-9, and blended-17 samples are progressively enhanced. The ultimate tensile strength, yield strength, and elongation of the blended-4 sample after the T6 heat treatment are 643 MPa, 607 MPa, and 13.5%, respectively. The corresponding values of the blended-9 sample after T6 heat treatment are 677 MPa, 615 MPa, and 12.5%, and those of the blended-17 sample after heat treatment are 690 MPa, 621 MPa, and 12%. It can be seen that the ultimate tensile strength and yield strength increase steadily with the extrusion ratio, while the decrease in elongation is slow.

4. Discussion

4.1. *Effects of oxygen content on microstructures*

By comparing the EBSD microstructures in Figs. 7, 9 and 11, it is found that the grain size and recrystallized microstructure of the blended-9 alloy and the ball-milled-9 alloy are significantly different. It should be noted that the apparent changes are mainly introduced by the different oxygen contents (0.15 wt% and 0.33 wt%) in the two alloys. First, after the same extrusion ratio, the evenly distributed precipitated phases of ball-milled-9 alloy (seen from Fig. 11(a)) are significantly smaller than those of blended-9 alloy (seen from Fig. 6(b)). As is well known, the secondary phases preferentially nucleate at grain boundaries with low interface energy. Many studies have reported that ball milling can increase the content of oxide film on the surface of aluminum powder, which can further form finer alumina particles and become uniformly dispersed in the matrix during the subsequent extrusion process. These particles can be used as recrystallization nucleation sites, resulting in small grains with more interfaces, more even dispersion and fine secondary phases. Zhao et al. [41] also demonstrated this microstructure characteristic by preparing nanocrystals via high-energy ball milling. Notably, the grains of ball-milled-9 alloy are obviously refined and the recrystallized texture is not changed after heat treatment. With the increase in oxygen content, the ball-milled-9 alloy still maintains the {111}<112> deformation texture after heat treatment (seen from Fig. 11(h)). This phenomenon can be explained by the Zener drag effect. The Zener pressure is proportional to $\gamma_{GB} \cdot V_f / r$, where γ_{GB} is the grain boundary energy, V_f is the particle volume fraction, and r is the average particle size [42]. It can be seen that fine dispersions tend to hinder the boundary motion and slow down the recrystallization and grain growth through the Zener drag effect. The study by Nikulin et al. [43] also showed that extensive grain refinement was obtained under ECAP when a dispersion of fine Al_6Mn particles was present in the Al–Mg–Mn alloy. The volume fraction of fine alumina particles in the ball-milled-9 alloy is higher, which means that it is more difficult for the recrystallization to occur in the ball-milled-9 alloy. On the whole, the increase in number of fine alumina particles caused by the increase in oxygen content can be attributed to the reduction in size of the secondary phases, the grain refinement, and the texture change.

4.2. *Strengthening mechanism*

The effects of the extrusion ratio of the blended alloy and oxygen content of the ball-milled alloys on the microstructure and mechanical properties were also analyzed. Multiple strengthening mechanisms contribute to the high strength of the Al–Zn–Mg–Cu alloys. The yield

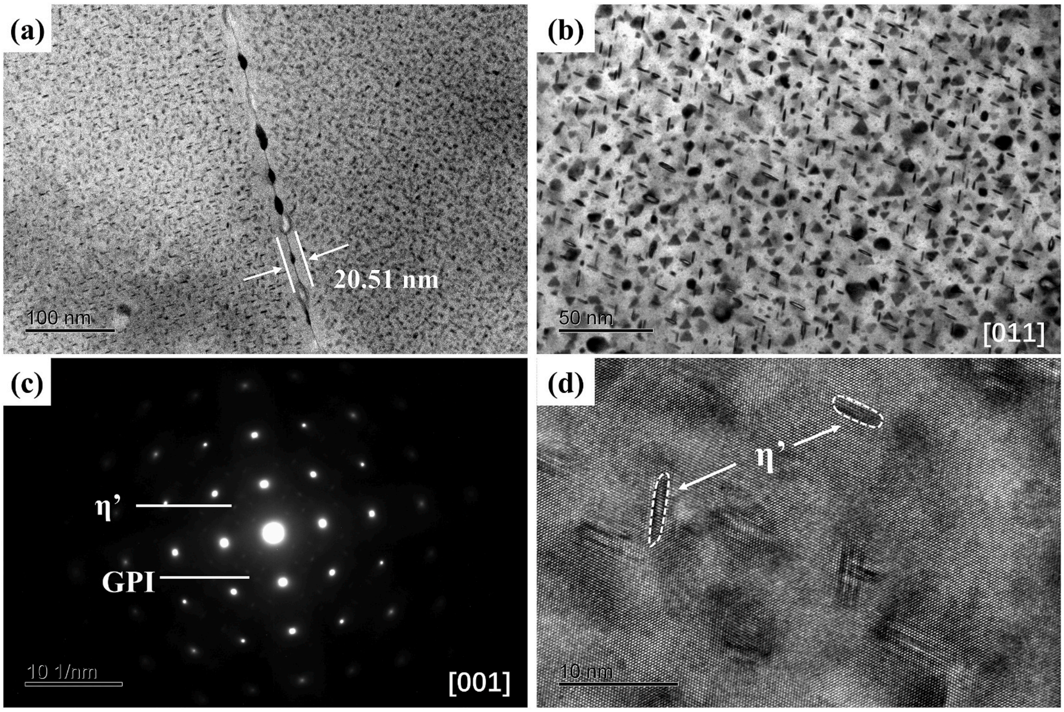

Fig. 13. TEM images of ball-milled-9 alloy after heat treatment: (a) precipitates, (b) intragranular precipitates along the [011] Al direction, (c) the corresponding selected area electron diffraction (SAED) patterns, and (d) the high-resolution transmission electron microscopy (HRTEM) image.

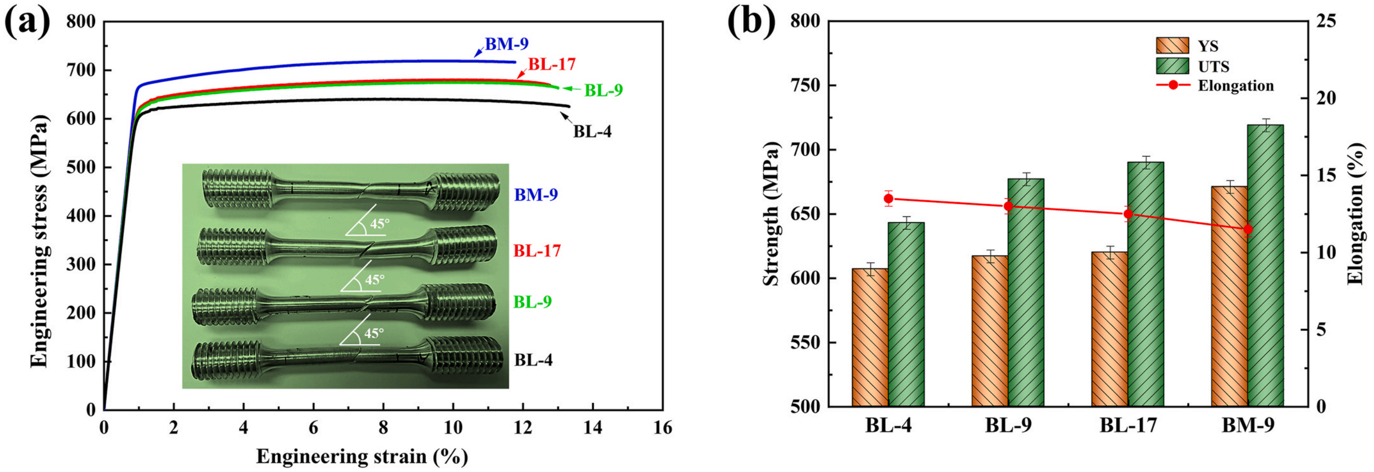

Fig. 14. (a) Engineering stress-strain curves and (b) mechanical properties of heat-treated blended-4, blended-9, blended-17, and ball-milled-9 alloys.

strength was calculated to confirm the main strengthening mechanisms of the precipitation-strengthened Al–Zn–Mg–Cu alloy [28]. Combined with the calculation formula of traditional Al–Zn–Mg–Cu alloy, it is inferred that powder metallurgy Al–Zn–Mg–Cu has the γ-Al_2O_3 dispersion strengthening mechanism. The yield strength ($\sigma_{\text{yield strength}}$) of the powder metallurgy Al–Zn–Mg–Cu alloy can be described by the sum of each strengthening component as follows:

$$\sigma_{\text{yield strength}} = \sigma_{\text{Al}} + \Delta\sigma_{\text{gb}} + \Delta\sigma_{\text{d}} + \Delta\sigma_{\text{ss}} + \Delta\sigma_{\text{ppt}} + \Delta\sigma_{\text{alumina}} \tag{1}$$

Here, σ_{Al} is the yield strength of pure Al (45 MPa [40]), and $\Delta\sigma_{\text{gb}}$, $\Delta\sigma_{\text{d}}$, $\Delta\sigma_{\text{ss}}$, $\Delta\sigma_{\text{ppt}}$, and $\Delta\sigma_{\text{alumina}}$ are the strength increments due to grain boundaries, dislocations, solid-solution, precipitates, and γ-Al_2O_3, respectively.

To compare the final performance of alloys with different extrusion ratios, the measured composition (traced back to the same sintered sample), and the T6 heat treatment conditions were kept consistent with the blended-4, blended-9, and blended-17 samples. It can be considered that the solid solution strengthening effect by the solute atoms and the strengthening effect of precipitation phases and Al_2O_3 have the same contribution to the strength of blended-4, blended-9, and blended-17 samples. The yield strength increment can be calculated as:

$$\Delta\sigma_{\text{yield strength}} = \Delta\sigma_{\text{gb}} + \Delta\sigma_{\text{d}} \tag{2}$$

Grain boundary strengthening ($\Delta\sigma_{\text{gb}}$) is generally described by the Hall-Petch equation [11]:

$$\Delta\sigma_{\text{gb}} = \text{k}\cdot\text{d}^{-1/2} \tag{3}$$

Here, d is the average grain size and k is 0.12 MPa $\text{m}^{-1/2}$ for the Al–Zn–Mg–Cu alloy [28]. The average grain sizes of the blended-4, blended-9, and blended-17 samples are 5.17 μm, 4.28 μm, and 3.83 μm, respectively. Grain boundary strengthening increases the yield strength of the blended-4, blended-9, and blended-17 samples by 52 MPa, 57 MPa, and 61 MPa, respectively.

Dislocation strengthening $\Delta\sigma_d$ can be calculated using the Bailey-Hirsch equation [44]:

$$\Delta\sigma_d = M\alpha Gb\rho^{1/2} \tag{4}$$

Here, M is the mean orientation factor of FCC metals (3.06), α is a constant (0.2 for FCC metals), G is the shear modulus (26.9 GPa for the Al–Zn–Mg–Cu alloy), b is the Burgers vector (0.286 nm for FCC Al), and ρ is the dislocation density composed of GNDs and statistically stored dislocations (SSDs) [45,46]. Previous studies [47] have confirmed that the dislocation strengthening effect of annealed alloys is mainly from the GNDs, as the density of retained SSDs is very low due to the recovery upon annealing. Lee et al. [11] confirmed that the total dislocation density value for Al–Zn–Mg–Cu is almost equal to ρ^{GND} due to the recovery during the solution treatment process. The density of GNDs can be calculated by the following expression [48]:

$$\rho = 2\theta/\mu b \tag{5}$$

Here, θ is the misorientation angle and μ is the unit length of 500 nm. The misorientation angle was estimated based on the KAM maps from the EBSD analysis. The calculated $\Delta\sigma_d$ values of blended-4, blended-9, and blended-17 samples are 82 MPa, 84 MPa, and 94 MPa, respectively. Therefore, the increments provided by grain boundary strengthening and dislocation strengthening are 134 MPa, 141 MPa, and 155 MPa. According to calculations, compared to the blended-4 sample, the increment in the yield strength of the blended-9 sample is 7 MPa, and that of the blended-17 sample is 14 MPa compared to the blended-9 sample. Thus, the theoretical values are consistent with the actual measured values.

To evaluate the specific contributions of each mechanism of the ball-milled-9 sample, the total strength $\sigma_{\text{yield strength}}$ of the alloy is described by Eq. (1). According to Eq. (3), the value of grain boundary strengthening $\Delta\sigma_{gb}$ of the ball-milled-9 alloy with average grain size of 2.62 μm is 74 MPa. The strength contributed by dislocations $\Delta\sigma_d$ with the dislocation density of $4.6 \times 10^{14}\ \text{m}^{-2}$ for the ball-milled-9 sample is estimated to be 101 MPa using Eq (4).

Solid solution strengthening occurs in the ball-milled-9 alloy under the T6 heat-treated state. However, due to the T6 heat treatment, a large number of atoms form the secondary phase, which reduces the number of atoms in solid solution in the matrix. Hence, the effect of solid solution strengthening can be ignored [49]. Previous reports [28] also revealed that the solid solution strengthening for the 7075 alloy can be up to 82 MPa, assuming that all these solute atoms are in a solid solution and the effects of various solutes are additive. However, a large number of the solute atoms are already precipitated. Thus, it can be concluded that the contribution of solid solution strengthening to the total strength is small.

The dislocation bypassing the Orowan mechanism is the operative strengthening mechanism for all of the precipitated particles in Al–Zn–Mg–Cu alloys, and the yield strength increment can be calculated as follows [40]:

$$\Delta\sigma ppt = \frac{MGb}{2\pi\sqrt{1-\nu}}\,\frac{\ln(\pi r/2b)}{\lambda} \tag{6}$$

Here, ν is the Poisson's ratio (0.33 for this alloy), r is the mean radius of precipitates, and λ is the edge-to-edge inter-precipitate spacing given by the following equation [40]:

$$\lambda = 2r\left(\sqrt{\frac{\pi}{3\sqrt{3}f_\nu}} - \frac{\pi}{4}\right) \tag{7}$$

Here, f_v is the volume fraction of precipitates. The values of r and f_ν are listed in Table 2. Therefore, the contribution of precipitation strengthening to yield strength is calculated to be 485 MPa.

Particle strengthening generally occurs through the Orowan mechanism. Oxide ceramic particles do not typically deform at room temperature, that is, these particles cannot be easily sheared by dislocations. Therefore, the Orowan bypass mechanism is also applicable to the γ-Al_2O_3 dispersion strengthening phase. Using the values in Table 2, the $\Delta\sigma_{alumina}$ value is calculated to be 35 MPa. However, due to the nonlinear superposition of γ-Al_2O_3 dispersion strengthening and precipitation strengthening, the actual strength provided is far less than 35 MPa. This value is only for reference and is not included in the sum.

5. Conclusions

In this paper, Al-8.3Zn-2.3Mg-2.5Cu alloys containing 0.15 wt% and 0.33 wt% oxygen, namely blended and ball-milled alloys, were prepared by powder mixing or ball milling, cold isostatic pressing, and vacuum sintering. Hot extrusion was carried out with 4:1, 9:1, and 17:1 extrusion ratios for the blended alloy and 9:1 extrusion ratio for the ball-milled alloy, followed by heat treatment. The effects of oxygen content and extrusion ratio on the microstructure and properties were studied in detail. The results are as follows:

(1) The increase in specific surface area of powder due to ball-milling results in higher oxygen content, and causes the sintered density of the ball-milled alloy (98.7%) to be slightly lower than that of the blended alloy (99.1%). Moreover, the grains of the ball-milled alloy (4.83 μm) are finer than those of the blended alloy (5.60 μm) due to the alumina film on the particle surface.

(2) With the increase in extrusion ratio, the secondary phase particles are broken up even more, and the average grain size decreases gradually. After heat treatment, the {111}<112> deformation texture changes to the {001}<001> and {001}<111> recrystallization textures.

(3) The yield strength values of the blended-4, blended-9, and blended-17 alloys after extrusion and heat treatment are 607 MPa, 615 MPa, and 621 MPa, respectively. The calculated increase in yield strength is mainly contributed by grain boundary strengthening.

(4) The average grain size of the ball-milled-9 alloy after extrusion is 2.17 μm, which becomes 2.62 μm after heat treatment. The {111}<112> deformation texture remains unchanged after heat treatment, which can be attributed to the strong hindering of dislocations and grain boundary migration by a large number of alumina particles.

(5) The ultimate tensile strength, yield strength, and elongation of heat-treated ball-milled-9 alloy are 719 MPa, 690 MPa, and 11.5%, respectively. It is calculated that the contributions of grain boundary strengthening, precipitation strengthening, and dislocation strengthening to the increase in yield strength are 74 MPa, 485 MPa, and 101 MPa, respectively.

CRediT authorship contribution statement

Weihao Han: Methodology, Validation, Investigation, Writing – original draft, Visualization. **Cunguang Chen:** Conceptualization, Methodology, Validation, Writing – review & editing, Funding acquisition. **Pei Li:** Formal analysis. **Yang Li:** Resources. **Guoping Su:** Resources. **Chunfang Sun:** Formal analysis. **Fang Yang:** Data curation. **Alex A. Volinsky:** Data processing, Paper corrections. **Zhimeng Guo:** Supervision, Funding acquisition.

Declaration of competing interest

The authors declare that they have no known competing financial interests or personal relationships that could have appeared to influence the work reported in this paper.

Data availability

No data was used for the research described in the article.

Acknowledgments

This work was supported by the National Natural Science Foundation of China (Grant Nos. 52271020, 92066205, U21A200305), the Science and Technology Innovation Special Fund Project of Foshan Municipal People's Government of China (Grant No. BK22BE007), the National Natural Science Foundation for Distinguished Young Scholars of China (Grant No. 51925401), and the Full-time Introduction of National High-level Innovative Talents Scientific Research Project in the Hebei Province of China (Grant No. 2021HBQZYCSB007).

References

[1] Y.X. Geng, D. Zhang, J.S. Zhang, L.Z. Zhuang, Early-stage clustering and precipitation behavior in the age-hardened Al–Mg–Zn(-Cu) alloys, Mater. Sci. Eng., A 856 (2022), 144015, https://doi.org/10.1016/j.msea.2022.144015.

[2] W.L. Wu, Y.L. Song, J. Lu, Y.Q. Yu, L. Hua, Novel strategy of electroshock treatment for improving mechanical performances of Al–Zn–Mg–Cu alloy by edge dislocation increment, Mater. Sci. Eng., A 854 (2022), 143805, https://doi.org/10.1016/j.msea.2022.143805.

[3] X.D. Wang, Q.L. Pan, W.Y. Wang, Z.Q. Huang, J. Chen, B.Q. Pan, X. Liu, Effects of pre-strain and aging treatments on the mechanical property and corrosion resistance of the spray formed ultra-high strength Al-Zn-Mg-Cu alloy, Mater. Char. 194 (2022), 112381, https://doi.org/10.1016/j.matchar.2022.112381.

[4] J. Tang, J.H. Wang, J. Teng, G. Wang, D.F. Fu, H. Zhang, F.L. Jiang, Effect of Zn content on the dynamic softening of Al-Zn-Mg-Cu alloys during hot compression deformation, Vacuum 184 (2021), 109941, https://doi.org/10.1016/j.vacuum.2020.109941.

[5] A. Ghosh, M. Ghosh, 3D FEM simulation of Al-Zn-Mg-Cu alloy during multi-pass ECAP with varying processing routes, Mater. Today Commun. 26 (2021), 102112, https://doi.org/10.1016/j.mtcomm.2021.102112.

[6] P. Dai, X. Luo, Y.Q. Yang, Z.D. Kou, B. Huang, C. Wang, J.X. Zang, J.G. Ru, Nano-scale precipitate evolution and mechanical properties of 7085 aluminum alloy during thermal exposure, Mater. Sci. Eng., A 729 (2018) 411–422, https://doi.org/10.1016/j.msea.2018.05.092.

[7] Y.H. Peng, C.Y. Liu, L.L. Wei, H.J. Jiang, Z.J. Ge, Quench sensitivity and microstructures of high-Zn-content Al-Zn-Mg-Cu alloys with different Cu contents and Sc addition, Trans. Nonferrous Metals Soc. China 31 (1) (2021) 24–35, https://doi.org/10.1016/S1003-6326(20)65476-0.

[8] J. Jiang, F. Jiang, M.H. Zhang, Z.Q. Tang, M.M. Tong, The recrystallization behavior of shear band in room temperature ECAPed Al-Mg-Mn-Sc-Zr alloy, Mater. Char. 175 (2021), 111081, https://doi.org/10.1016/j.matchar.2021.111081.

[9] M.A. Afifi, Y.C. Wang, P.H.R. Pereira, Y. Huang, Y.W. Wang, X.W. Cheng, S.K. Li, T. G. Langdon, Effect of heat treatments on the microstructures and tensile properties of an ultrafine-grained Al-Zn-Mg alloy processed by ECAP, J. Alloys Compd. 749 (2018) 567–574, https://doi.org/10.1016/j.jallcom.2018.03.206.

[10] M. Elhefnawey, G.L. Shuai, Z. Li, D.T. Zhang, M.M. Tawfik, L. Li, On achieving ultra-high strength and improved wear resistance in Al-Zn-Mg alloy via ECAP, Tribol. Int. 163 (2021), 107188, https://doi.org/10.1016/j.triboint.2021.107188.

[11] S.H. Lee, J.G. Jung, S.I. Baik, D.N. Seidman, M.S. Kim, Y.K. Lee, K. Euh, Precipitation strengthening in naturally aged Al-Zn-Mg-Cu alloy, Mater. Sci. Eng., A 803 (2021), 140719, https://doi.org/10.1016/j.msea.2020.140719.

[12] F.H. Cao, J.X. Zheng, Y.J. Jiang, B. Chen, Y.R. Wang, T. Hu, Experimental and DFT characterization of η' nano-phase and its interfaces in AlZnMgCu alloys, Acta Mater. 164 (2019) 207–219, https://doi.org/10.1016/j.actamat.2018.10.045.

[13] D.M. Liu, B.Q. Xiong, F.G. Bian, Z.H. Li, X.W. Li, Y.A. Zhang, Q.S. Wang, G.L. Xie, F. Wang, H.W. Liu, Quantitative study of nanoscale precipitates in Al-Zn-Mg-Cu alloys with different chemical compositions, Mater. Sci. Eng., A 639 (2015) 245–251, https://doi.org/10.1016/j.msea.2015.04.104.

[14] M.M. Sharma, M.F. Amateau, T.J. Eden, Aging response of Al–Zn–Mg–Cu spray formed alloys and their metal matrix composites, Mater. Sci. Eng., A 424 (1–2) (2006) 87–96, https://doi.org/10.1016/j.msea.2006.02.047.

[15] F. Wang, B.Q. Xiong, Y.A. Zhang, B.H. Zhu, H.W. Liu, X.Q. He, Effect of heat treatment on the microstructure and mechanical properties of the spray-deposited Al-10.8Zn-2.8Mg-1.9Cu alloy, Mater. Sci. Eng., A 486 (1–2) (2008) 648–652, https://doi.org/10.1016/j.msea.2007.09.049.

[16] H.C. Li, F.Y. Cao, S. Guo, Y.D. Jia, D.Y. Zhang, Z.Y. Liu, P. Wang, S. Scudino, J. F. Sun, Effects of Mg and Cu on microstructures and properties of spray-deposited Al-Zn-Mg-Cu alloys, J. Alloys Compd. 719 (2017) 89–96, https://doi.org/10.1016/j.jallcom.2017.05.101.

[17] A. Ditta, L.J. Wei, Y.J. Xu, S.J. Wu, Effect of hot extrusion and optimal solution treatment on microstructure and properties of spray-formed Al-11.3Zn-2.65Mg-1Cu alloy, J. Alloys Compd. 797 (2019) 558–565, https://doi.org/10.1016/j.jallcom.2019.05.057.

[18] S. Devaraj, S. Sankaran, R. Kumar, G.A. Rao, Influence of hot isostatic pressing on the microstructure and mechanical properties of a spray-formed Al-4.5 wt.% Cu Alloy, J. Mater. Eng. Perform. 23 (2014) 1440–1450, https://doi.org/10.1007/s11665-014-0869-z.

[19] M.A. Valdes-Tabernero, R. Sancho-Cadenas, I. Sabirov, M.Y. Murashkin, I. A. Ovid'ko, F. Galvez, Effect of SPD processing on mechanical behavior and dynamic strain aging of an Al-Mg alloy in various deformation modes and wide strain rate range, Mater. Sci. Eng., A 696 (2017) 348–359, https://doi.org/10.1016/j.msea.2017.04.024.

[20] Y.D. Zhang, S.B. Jin, P.W. Trimby, X.Z. Liao, M.Y. Murashkin, R.Z. Valiev, J.Z. Liu, J.M. Cairney, S.P. Ringer, G. Sha, Dynamic precipitation, segregation and strengthening of an Al-Zn-Mg-Cu alloy (AA7075) processed by high-pressure torsion, Acta Mater. 162 (2019) 19–32, https://doi.org/10.1016/j.actamat.2018.09.060.

[21] J. Zhao, Y. Deng, J. Zhang, Z. Ma, Y. Zhang, Effect of temperature and strain rate on the grain structure during the multidirectional forging of the Al-Zn-Mg-Cu alloy, Mater. Sci. Eng., A 756 (2019) 119–128, https://doi.org/10.1016/j.msea.2019.04.033.

[22] M.Z. Quadir, N. Najafzadeh, P.R. Munroe, Variations in through-thickness recrystallization and grain growth textures in the Al layers in ARB-processed Al/Al (0.3% Sc) composite sheets, Mater. Des. 93 (2016) 467–473, https://doi.org/10.1016/j.matdes.2015.12.106.

[23] P. Hidalgo-Manrique, A. Orozco-Caballero, C.M. Cepeda-Jiménez, O.A. Ruano, F. Carreño, Influence of the accumulative roll bonding process severity on the microstructure and superplastic behaviour of 7075 Al Alloy, J. Mater. Sci. Technol. 32 (8) (2016) 774–782, https://doi.org/10.1016/j.jmst.2016.06.004.

[24] W.Y. Wang, Q.L. Pan, X.D. Wang, Y.W. Sun, L. Long, Z.Q. Huang, Mechanical properties and microstructure evolution of ultra-high strength Al-Zn-Mg-Cu alloy processed by room temperature ECAP with post aging, Mater. Sci. Eng., A 731 (2018) 195–208, https://doi.org/10.1016/j.msea.2018.06.047.

[25] M.V. Markushev, E.V. Avtokratova, S.V. Krymskiy, O.S. Sitdikov, Effect of precipitates on nanostructuring and strengthening of high-strength aluminum alloys under high pressure torsion, J. Alloys Compd. 743 (2018) 773–779, https://doi.org/10.1016/j.jallcom.2018.02.047.

[26] C.G. Chen, W.H. Han, M. Qi, S.P. Dong, P. Li, F. Yang, J.J. Hao, Z.M. Guo, Microstructural evolution and mechanical properties of an ultrahigh-strength Al−Zn−Mg−Cu alloy via powder metallurgy and hot extrusion, J. Cent. South Univ. 28 (2021) 1195–1205, https://doi.org/10.1007/s11771-021-4669-y.

[27] M. Balog, P. Krizik, M. Yan, F. Simancik, G.B. Schaffer, M. Qian, SAP-like ultrafine-grained Al composites dispersion strengthened with nanometric AlN, Mater. Sci. Eng., A 588 (2013) 181–187, https://doi.org/10.1016/j.msea.2013.09.027.

[28] M. Balog, P. Krizik, O. Bajana, T. Hu, H. Yang, J.M. Schoenung, E.J. Lavernia, Influence of grain boundaries with dispersed nanoscale Al_2O_3 particles on the strength of Al for a wide range of homologous temperatures, J. Alloys Compd. 772 (2019) 472–481, https://doi.org/10.1016/j.jallcom.2018.09.164.

[29] K.K. Ma, H.M. Wen, T. Hu, T.D. Topping, D. Isheim, D.N. Seidman, E.J. Lavernia, J. M. Schoenung, Mechanical behavior and strengthening mechanisms in ultrafine grain precipitation-strengthened aluminum alloy, Acta Mater. 62 (2014) 141–155, https://doi.org/10.1016/j.actamat.2013.09.042.

[30] S.M.S. Aghamiri, N. Oono, S. Ukai, R. Kasada, H. Noto, Y. Hishinuma, T. Muroga, Microstructure and mechanical properties of mechanically alloyed ODS copper alloy for fusion material application, Nucl. Mater. Energy 15 (2018) 17–22, https://doi.org/10.1016/j.nme.2018.05.019.

[31] R. Singh, U. Prakash, D. Kumar, K. Laha, Nano oxide particles in 18Cr oxide dispersion strengthened (ODS) steels with high yttria contents, Mater. Char. 189 (2022), 111936, https://doi.org/10.1016/j.matchar.2022.111936.

[32] Y. Dong, X.K. Wang, Y.H. Xie, C. Yang, D.S. Zhou, Tunable microstructures and tensile mechanical properties of oxide-dispersion-strengthened Cu by extrusion and secondary processing, J. Alloys Compd. 812 (2020), 152112, https://doi.org/10.1016/j.jallcom.2019.152112.

[33] K. Han, R.E. Goddard, V. Toplosky, R. Niu, J. Lu, R. Walsh, Alumina particle reinforced Cu matrix conductors, IEEE Trans. Appl. Supercond. 28 (3) (2018) 1–5, https://doi.org/10.1109/TASC.2018.2795587.

[34] R.N. Lumley, G.B. Schaffer, Anomalous pore morphologies in liquid phase sintered aluminium-zinc alloys, Metall. Mater. Trans. A 55 (10) (2000) 45, https://doi.org/10.1016/S0026-0657(00)80071-5.

[35] G.B. Schaffer, T.B. Sercombe, R.N. Lumley, Liquid phase sintering of aluminium alloys, Mater. Chem. Phys. 67 (1–3) (2001) 85–91, https://doi.org/10.1016/S0254-0584(00)00424-7.

[36] C.G. Chen, F. Li, W.H. Han, T.X. Lu, P. Li, Q.Y. Cui, Y.L. Sui, Z.M. Guo, A. A. Volinsky, Thermally stable Al conductor prepared from Al powder with a low oxygen content, Mater. Sci. Eng., A 813 (2021), 141174, https://doi.org/10.1016/j.msea.2021.141174.

[37] H.Y. Xiao, Y.G. Li, J.W. Geng, H.P. Li, M.L. Wang, D. Chen, Z.G. Li, H.W. Wang, Effects of nano-sized TiB_2 particles and Al_3Zr dispersoids on microstructure and mechanical properties of Al-Zn-Mg-Cu based materials, T NONFERR METAL SOC 31 (8) (2021) 2189–2207, https://doi.org/10.1016/S1003-6326(21)65648-0.

[38] F.H. Shen, W.F. Li, Z.Z. Sun, Z.R. Zhou, C.X. Xie, Z.L. Liao, D.Q. Yi, Insights of texture and microstructure evolution in the short time annealing of Al-Cu-Mg alloy at large temperature range, J. Alloys Compd. 871 (2021), 159613, https://doi.org/10.1016/j.jallcom.2021.159613.

[39] W.X. Shu, L.G. Hou, C. Zhang, F. Zhang, J.C. Liu, J.T. Liu, L.Z. Zhuang, J.S. Zhang, Tailored Mg and Cu contents affecting the microstructures and mechanical properties of high-strength Al-Zn-Mg-Cu alloys, Mater. Sci. Eng., A 657 (2016) 269–283, https://doi.org/10.1016/j.msea.2016.01.039.

[40] J. Ren, R.C. Wang, C.Q. Peng, Y. Feng, Multistage aging treatment influenced precipitate characteristics improve mechanical and corrosion properties in powder

hot-extruded 7055 Al alloy, Mater. Char. 170 (2020), 110683, https://doi.org/10.1016/j.matchar.2020.110683.

[41] K.Y. Zhao, C.J. Li, J.M. Tao, Dickon H.L. Ng, X.K. Zhu, The synthesis, microstructure, hardness and thermal properties of bulk nanocrystalline Al produced by in situ consolidation with low-energy ball milling, J. Alloys Compd. 504 (2010) S306–S310, https://doi.org/10.1016/j.jallcom.2010.03.204.

[42] K. Huang, R.E. Logé, A review of dynamic recrystallization phenomena in metallic materials, Mater. Des. 111 (2016) 548–574, https://doi.org/10.1016/j.matdes.2016.09.012.

[43] I. Nikulin, A. Kipelova, S. Malopheyev, R. Kaibyshev, Effect of second phase particles on grain refinement during equal-channel angular pressing of an Al–Mg–Mn alloy, Acta Mater. 60 (2) (2012) 487–497, https://doi.org/10.1016/j.actamat.2011.10.023.

[44] S.V. Zherebtsov, G.S. Dyakonov, A.A. Salem, V.I. Sokolenko, G.A. Salishchev, S. L. Semiatin, Formation of nanostructures in commercial-purity titanium via cryorolling, Acta Mater. 61 (4) (2013) 1167–1178, https://doi.org/10.1016/j.actamat.2012.10.026.

[45] E. Demir, D. Raabe, N. Zaafarani, S. Zaefferer, Investigation of the indentation size effect through the measurement of the geometrically necessary dislocations beneath small indents of different depths using EBSD tomography, Acta Mater. 57 (2) (2009) 559–569, https://doi.org/10.1016/j.actamat.2008.09.039.

[46] H. Mughrabi, Deformation-induced long-range internal stresses and lattice plane misorientations and the role of geometrically necessary dislocations, Philos. Mag. A 86 (25–26) (2006) 4037–4054, https://doi.org/10.1080/14786430500509054.

[47] Z.W. Wang, W.J. Lu, H. Zhao, C.H. Liebscher, J.Y. He, D. Ponge, D. Raabe, Z.M. Li, Ultrastrong lightweight compositionally complex steels via dual-nanoprecipitation, Sci. Adv. 6 (2020), https://doi.org/10.1126/sciadv.aba9543 eaba9543.

[48] Z.F. Yan, D.H. Wang, X.L. He, W.X. Wang, H.X. Zhang, P. Dong, C.H. Li, Y.L. Li, J. Z. Zhou, Z. Liu, L.Y. Sun, Deformation behaviors and cyclic strength assessment of AZ31B magnesium alloy based on steady ratcheting effect, Mater. Sci. Eng., A 723 (2018) 212–220, https://doi.org/10.1016/j.msea.2018.03.023.

[49] K.K. Ma, T. Hu, H. Yang, T. Topping, A. Yousefiani, E.J. Lavernia, J.M. Schoenung, Coupling of dislocations and precipitates: impact on the mechanical behavior of ultrafine grained Al-Zn-Mg alloys, Acta Mater. 103 (2016) 153–164, https://doi.org/10.1016/j.actamat.2015.09.017.